A bispecific monomeric nanobody induces SARS-COV-2 spike trimer dimers

Leo Hanke[1,†], Hrishikesh Das[2,†], Daniel J Sheward[1], Laura Perez Vidakovics[1], Egon Urgard[1], Ainhoa Moliner-Morro[1], Vivien Karl[1], Alec Pankow[1], Changil Kim[1], Natalie L Smith[1,] Gabriel K Pedersen[3], Jonathan M Coquet[1], B Martin Hällberg[2,4,*], Ben Murrell[1,‡,*], Gerald M McInerney[1, ‡,*]

[1] Department of Microbiology, Tumor and Cell Biology, Karolinska Institutet, Stockholm, Sweden.

[2] Department of Cell and Molecular Biology, Karolinska Institutet, Stockholm, Sweden.

[3] Center for Vaccine Research, Statens Serum Institut, Copenhagen, Denmark

[4] Karolinska Institutet VR-RÅC, Centre for Structural Systems Biology, Notkestraße 85, 22607, Hamburg, Germany

[†] Contributed equally

[‡] Contributed equally

* Correspondence to: martin.hallberg@ki.se; benjamin.murrell@ki.se; gerald.mcinerney@ki.se

Abstract

Antibodies binding to the severe acute respiratory syndrome coronavirus 2 (SARS-CoV-2) spike have therapeutic promise, but emerging variants show the potential for virus escape. Thus, there is a need for therapeutic molecules with distinct and novel neutralization mechanisms. Here we isolated a nanobody that potently neutralizes SARS-CoV-2, including the B.1.351 variant, and cross-neutralizes SARS-CoV. We demonstrate the therapeutic potential of the nanobody in a human ACE2 transgenic mouse model. Using biochemistry and electron cryomicroscopy we show that this nanobody simultaneously interacts with two RBDs from different spike trimers, rapidly inducing the formation of spike trimer-dimers. This naturally elicited bispecific monomeric nanobody establishes a novel strategy for potent immobilization of viral antigens.

Introduction

The SARS-CoV-2 pandemic and the vast societal and economic consequences of the connected lockdowns have had devastating consequences for the world's populations. Despite rapid progress in vaccine development, some emerging virus variants appear to be less effectively neutralized by antibodies elicited by the first-generation vaccines [1] and the emergence of further variants is expected. To prepare for different scenarios and to have emergency alternatives at hand, novel ways to inhibit and neutralize the virus and variants of concern are needed. As therapeutic agents in the early phases of SARS-CoV-2 infection, camelid-derived single-domain antibody fragments are promising candidates. These so-called 'nanobodies' not only bind their antigen with very high specificity and affinity, but they can also be easily produced to large quantities in *E.coli* [2] and show favourable biochemical characteristics, including good thermal

53 stability. Importantly, they can easily be combined to form homo- and heterodimers or other
54 multimers to increase potency and target multiple epitopes simultaneously [3–5]. This strategy
55 allows the neutralization of multiple known or unknown virus variants and reduces the risk for
56 viral escape [5].
57 The attachment of SARS-CoV-2 to the host cell receptor ACE2 and subsequent membrane
58 fusion is mediated by the viral spike (S) protein [6]. In the prefusion conformation, the spike is a
59 large homotrimer. Each S monomer consists of two subunits: S1 and S2. The S1 subunit contains
60 the receptor binding domain (RBD) and S2 contains the fusion peptide, as well as the
61 transmembrane domain. The RBD is responsible for the initial attachment to ACE2 and is found
62 in two distinct conformational states: The receptor-accessible 'up' conformation and the receptor
63 inaccessible 'down' conformation [6,7]. Receptor binding induces the rather unstable 3-up state,
64 which leads to shedding of S1 and refolding of S2 thereby presenting the fusion peptide to the
65 opposing membrane [6,8,9]. SARS-CoV-2 is easily neutralized by high-affinity binding antibodies
66 and other spike-targeting molecules, including nanobodies [10–13]. Many of them bind to, or close
67 to, the receptor binding motif of the RBD and neutralize by directly hindering virus attachment
68 [14,15]. Other mechanisms include locking the RBDs in the down conformation or preventing
69 productive fusion [5,16]. Still, the emergence of new virus variants that evade antibody-mediated
70 neutralization mandates the identification of molecules with a more diverse set of binding
71 epitopes and neutralization mechanisms allowing for neutralization of a variety of virus variants.
72 Here, we generated a nanobody that has two non-overlapping interaction sites on the SARS-
73 CoV-2 RBD, each targeting a different epitope, which induces the formation of dimers of spike
74 trimers and suppresses SARS-CoV-2 *in vivo*.
75
76

77 **Results**

78 **Isolation and characterization of a potent RBD-specific nanobody.**

79 To identify nanobodies with unique neutralization potential, we immunized one alpaca (*Funny*)
80 with SARS-CoV-2 spike protein and recombinant RBD. We isolated RNA from peripheral blood
81 mononuclear cells and created phagemid libraries. Phage display screens with immobilized RBD
82 yielded one promising nanobody, called Fu2. Since multimerization of nanobodies can
83 substantially improve virus neutralization potency [3,17], we created three different dimers
84 (illustrated in Fig. 1A): One Fu2-Fc fusion, expressed in mammalian cells, the second a
85 chemically linked Fu2 homodimer, and thirdly a heterodimer of Fu2 with a previously described
86 RBD-specific neutralizing nanobody Ty1 [14]. Chemically linked constructs were generated using
87 a combination of sortase A labelling and Cu-free click-chemistry as described in detail
88 previously [3].

89 Using pseudotyped lentivirus (PSV) neutralization assay (Fig. 1B), we found that monomeric
90 Fu2 was approximately 10-times more potent than Ty1, with an IC_{50} in the range of 106 ng/ml (7
91 nM). The Fu2-Fc fusion only slightly increased the neutralization potency of this nanobody to 61
92 ng/ml (0.75 nM), and a chemical homo-dimerization to an IC_{50} of 26 ng/ml (0.8 nM). Thus, the
93 observed enhancement in potency is attributable to dimerization, rather than the Fc-domain itself.
94 Interestingly, the Fu2-Ty1 heterodimer was extremely potent, with an IC_{50} approximately 6-fold
95 lower than that of the Fu2 homodimer, in the range of 4 ng/ml (140 pM). Fu2 directly prevented
96 spike binding to ACE2 as confirmed by flow cytometry of HEK293T-hACE2 cells stained with
97 recombinant, fluorescently labelled spike (+/- Fu2) (Fig. 1C). Analysis of binding kinetics by
98 surface plasmon resonance (SPR) revealed that Fu2 bound the RBD with sub-nanomolar affinity
99 (Fig. 1D). The 1:1 binding model fit the sensorgrams well at the used concentration range,
100 indicating a single dominant interaction. Analysis of next-generation sequencing data for other

101 members of the Fu2 lineage yielded several Fu2-variants with similar properties (Supplementary
102 Fig. 1A-E).
103 To test the integrity of the recombinant spike protein after the addition of Fu2, we analysed the
104 size-exclusion chromatography elution profiles in combination with different nanobody
105 constructs (Fig. 1E). The SARS-CoV-2 spike trimer eluted in a single peak and the addition of
106 Ty1 [14] did not result in a shift in the position of this peak, which is expected given the small
107 relative size addition of the 14 kDa nanobody to the large (>400 kDa) spike trimer. In contrast,
108 the addition of Fu2 resulted in a substantial shift of the peak, suggesting the formation of a larger
109 complex, likely a dimer of the spike trimer. Next, we combined the spike with the Fu2-Ty1
110 heterodimer. This also resulted in earlier elution, and besides a possible spike dimer, this
111 construct gave rise to an even earlier elution peak suggesting the induction of higher-order spike
112 multimers.
113
114 **Structural basis for Fu2 induction of spike trimer dimers.**
115 To better understand neutralization and the aggregation of spike by Fu2, we used electron
116 cryomicroscopy (cryo-EM) to determine the structure of the Fu2-spike complex. The structure
117 revealed a remarkable head-to-head dimerization of the trimeric spike, bound by six molecules of
118 Fu2 (Fig. 2). This distinct structural state appeared as prominent 2D classes in our analyses (Fig.
119 2A). Binding of Fu2 to the RBD is unique as it can simultaneously interact with two different
120 RBDs from different spike trimers in the up conformation (Figs. 2B and 2C). To our knowledge,
121 Fu2 is the only nanobody or spike-binding molecule developed against the SARS-CoV-2 spike
122 to have this property. Our high resolution (2.9Å; 0.143 FSC) localized reconstruction of the
123 RBD-Fu2-RBD-Fu2 interface helped us elucidate the molecular details of this interaction. Each
124 RBD in the complex provides two binding interfaces for two Fu2 molecules, which we call

125 ‘interface-major’ and ‘interface-minor’ according to surface area covered (Fig. 2D and
126 Supplementary Fig 2A and Supplementary 2B). The interface-major and interface-minor have a
127 buried surface area of ~740 $Å^2$ and ~495 $Å^2$, respectively. Parts of the Fu2 framework regions
128 drive the dimerization by shape-complementarity and coupled solvent exclusion in the two
129 interfaces. In addition, the interface-major consists of 15 hydrogen bonds and one salt bridge
130 between Fu2 D117 and RBD K378, while the interface-minor comprises five hydrogen bonds.
131 Furthermore, a region around the Fu2 β-turn A40-K43 plays a key role in dimerization through
132 interactions with two proximal RBDs (Supplementary Figs. 2C and 2D). Specifically, one of the
133 two proximal RBDs’ T500-Y505 region packs against the Fu2 A40-K43 β-turn and the RBD
134 Y505 is in addition bound by Fu2 Q39. Meanwhile, the other proximal RBD is bound through a
135 bidentate hydrogen bond between Fu2 E44 and the backbone amides of RBD V503-G504 (Fig.
136 2E and Supplementary Figs. 2C and 2D). Interestingly, the overall structure of Fu2-bound spike
137 had no significant deviations from previous structures (Supplementary Fig. 3) and we did not find
138 any contact between any two Fu2 molecules or between spike trimers suggesting that the
139 observed spike trimer dimerization is solely driven RBD-Fu2 interactions.
140

141 **Fu2 blocks the RBD from binding ACE2.**

142 Structural alignment of an ACE2-RBD structure to the Fu2-spike structure (single RBD) shows
143 that binding of ACE2 would be hindered by Fu2 bound to any of the two interfaces (Fig. 2F).
144 Fu2 bound to the interface-major would clash with ACE2 residues ~303-331 and the N-glycan at
145 position 322, while Fu2 bound to interface-minor would mask the interaction surface of ACE2,
146 making it sterically impossible for ACE2 to access the RBD. A comparison of the Fu2 and Ty1
147 binding site revealed that interface-minor is partially shared between Ty1 and Fu2 (Supplementary
148 Figs. 2E and 2F), suggesting that in context of the Fu2-Ty1 heterodimer, Ty1 is displaced upon

149 dimerization of the spike trimer. Ty1 can then potentially bind additional spike molecules,
150 explaining the elution profile showing both dimers and higher order spike complexes (Fig. 1E).
151 In the complex, Fu2's long CDR3 (G99 to Y120) plays a significant role in RBD binding. Here,
152 the Fu2 S107-R111 region adopts a β-strand conformation that binds the RBD T376-Y380 β-
153 strand to give rise to an energetically favourable inter-chain extension of the RBD anti-parallel
154 β-sheet (Figs. 2G and 2H). Interestingly, the Fu2 CDR1 (G26-Y32) and CDR2 (T52-S57) do not
155 participate in RBD binding, and none of the CDRs is directly involved in the formation of the
156 spike dimer.
157
158 **Fu2 stabilizes the RBD in the 'up' conformation.**
159 Cryo-EM analyses, both of the purified spike or of intact virions has revealed that unliganded
160 spike is mostly present in all-down (~60%) or 1-up (~40%) conformation [6]. Our Fu2-spike
161 structure shows the presence of two trimeric spike molecules, both in the 3-up conformation.
162 This arrangement allows Fu2 to access all six possible binding sites on RBDs without steric
163 conflict. Alignment of RBD-Fu2 to RBD-down in a 2-up spike structure confirms that binding of
164 Fu2 to RBD in the down conformation is not possible (Supplementary Fig. 2G). Fu2 bound to
165 either interaction interface on an RBD in the down conformation would clash with neighbouring
166 RBDs. Likewise, an alignment of the 2-up spike structure to the Fu2-trimer-dimer shows that
167 RBD-down would clash with the neighbouring Fu2 molecule (Supplementary Fig. 2H). In
168 conclusion, for Fu2 binding and for trimer-dimer assembly, all RBDs must be in the up
169 conformation.
170
171 **Fu2-Ty1 provides therapeutic relief in a mouse model of SARS-CoV-2 infection**

172 An important requirement for the development of antivirals is neutralization potential *in vivo*. To
173 address this, we used K18-hACE2 transgenic mice that express human ACE2 as a model for
174 SARS-CoV-2 infection. To determine if neutralizing nanobodies could prevent infection, or
175 reduce disease severity when administered in early infection, we performed a prophylactic and a
176 therapeutic experiment *in vivo* (Fig. 3). Mice in the prophylactic treatment group (N=4) were
177 injected intraperitoneally (i.p.) with 370 µg of the Fu2-Ty1 heterodimer (11-20 mg/kg), 6 h
178 before intranasal challenge with 10^3 plaque forming units (PFU) of SARS-CoV-2. The
179 therapeutic group (N=4) was injected i.p. with 280 µg (9-14 mg/kg) of Fu2-Ty1 daily, for four
180 days, starting 24 h post infection. Viability and weight change were monitored daily for 12 days
181 post-challenge. Weight loss for infected mice was first observed on day 4. Prophylactic treatment
182 did not greatly alter weight loss or disease severity. In contrast, weight loss was delayed in mice
183 receiving Fu2-Ty1 heterodimers on a therapeutic regimen (10% weight loss endpoint, $p<0.05$,
184 Cox Proportional Hazard model). One of four mice treated post infection fully recovered from
185 infection with an otherwise-lethal challenge dose, with weight rebounding to pre-infection levels.
186 From day 6 oropharyngeal samples, qPCR of SARS-CoV-2 E-gene showed significantly reduced
187 genomic and subgenomic RNA in the therapeutic group compared to the untreated (Fig. 3C). The
188 data shows that the Fu2-Ty1 dimer suppresses SARS-CoV-2 *in vivo*.
189

190 **Fu2 cross-neutralizes SARS-CoV, and clinical isolates of SARS-CoV-2 including the**
191 **B.1.351 variant of concern**

192 To test the breadth of neutralization, we evaluated cross-neutralization of SARS-CoV PSV (Fig.
193 4A). While Ty1 did not neutralize SARS-CoV, Fu2 and dimeric Fu2 constructs were
194 neutralizing, but less so than against SARS-CoV-2 PSV. Interestingly, the neutralization curves
195 displayed a much flatter slope as compared to those against SARS-CoV-2 PSV. It required 6.1

196 μg /ml of monomeric Fu2 to reach 50% neutralization in this assay, while 570 ng /ml of Fu2-Fc
197 and 57 ng/ml of the Fu2-dimer was sufficient for 50% neutralization.
198 To understand the molecular mechanism of cross-neutralization of SARS-CoV we compared the
199 RBD sequences and performed structural alignments (Figs. 4B, 4C and Supplementary Fig. 4A).
200 Interestingly, the interface-major residues are conserved, while interface-minor has significant
201 differences, suggesting that the divergent interface-minor of SARS-CoV RBD would not permit
202 Fu2 binding. From these analyses we conclude that Fu2 binding would be unlikely to form
203 SARS-CoV trimer dimers.
204 To demonstrate neutralization of replication competent SARS-CoV-2 we performed a plaque
205 reduction neutralization test (PRNT) using infectious SARS-CoV-2, isolated from the first
206 Swedish COVID-19 patient [18] (Fig. 4D). Similar to neutralization of PSV, monomeric Fu2
207 neutralized SARS-CoV-2 much better than Ty1, a dimeric construct of Fu2 provided a 2.8-fold
208 improvement over the monomeric version of Fu2, while the heterodimer of Ty1 and Fu2 showed
209 a 50-fold improvement compared to monomeric Fu2 in this assay.
210 A PRNT using the B.1.351 (501Y.V2) [1] variant showed that Fu2 very potently neutralized this
211 novel variant (Fig. 4E) and that the Fu2 dimer and Fu2-Fc again improved neutralization
212 efficiency. The IC_{50} values were even slightly better than when using the Swedish isolate, but the
213 difference is within the intraassay variability. Ty1 failed to neutralize this virus, and the Fu2-Ty1
214 heterodimer did not neutralize better than Fu2 alone. The variant B.1.351 harbours four amino
215 acid substitutions in the RBD at position K417N, N439K, E484K and N501Y. Only N501 and
216 E484 are located in proximity of the Fu2 interaction interface. *In silico* analyses with the PISA
217 server (25) confirmed that the two interfaces do not change in these mutants. Both buried surface
218 areas of the interfaces as well as the number of possible hydrogen bonds remain unchanged (Fig.

219 4F). These results and analysis combined suggests that Fu2 likely also neutralizes the recently
220 emerged variants P1 (K417T, E484K, N501Y) and B.1.1.7 (N501Y).
221
222 **Discussion**
223 Nanobodies represent a valuable alternative to monoclonal antibodies for virus neutralization
224 [19,20]. Their ease of production, thermal stability, and robust biochemical behaviour, combined
225 with straight-forward functionalization and multimerization possibilities, make them suitable
226 candidates for therapeutic applications.
227 The newly emerged SARS-CoV-2 B.1.351 variant shows nine amino acid changes in the spike
228 protein. While biological properties of this variant remain to be determined, two amino acid
229 substitutions in the receptor binding motif are of potential concern for vaccine efficacy,
230 neutralization efficiency of existing monoclonal antibody therapies, and changed dynamics of
231 virus spread [21–23]. The novel nanobody described here, Fu2, can effectively neutralize the
232 B.1.351 variant and has therefore a strong and unique potential to form the basis for development
233 of therapeutic interventions against this emerging variant of concern.
234 Fu2 is also capable of neutralizing SARS-CoV, highlighting its specificity for a more conserved
235 epitope. However, the potency was significantly reduced for the monomeric nanobody, likely
236 because of decreased affinity to the RBD of this virus. That the dimeric constructs significantly
237 increased potency further supports this hypothesis. A similar observation was made for VHH-72
238 originally developed against SARS-CoV, but with some neutralization potential in dimeric form
239 against SARS-CoV-2 [24].
240 Nanobodies typically have short serum half-lives, ranging from 1-3 hours [25], compared to 6-8
241 days of IgG1 [26]. We show that a high dose of nanobody heterodimer is not suitable as a molecule
242 for passive immunization as it did not diminish the severity of disease of hACE2 expressing

243 mice. In contrast, if administered daily for four days post challenge, the heterodimer significantly
244 delayed disease onset and severity, suggesting that nanobodies and dimeric nanobody constructs
245 have the potential for SARS-CoV-2 antiviral therapy. Half-life extending strategies such as
246 fusion to serum albumin moieties could be used to extend half-life [27] and reduce the number of
247 infusions.
248 The RBD-specific nanobody Fu2 displays a particularly unique mode of virus neutralization by
249 rapidly inducing stable spike trimer dimers that are incapable of binding to ACE2. In contrast to
250 spike trimer dimers reported for the full-length spike that are based on S1-S1 interactions placing
251 the trimers 'side-by-side' [28], Fu2 induced a dimer in a 'head-to-head' orientation with the C-
252 termini at the distal ends. Targeting two epitopes increases the binding surface area, but, more
253 importantly, when locked in such a conformation the function of each glycoprotein is sterically
254 blocked both by the nanobody and by the other glycoprotein in such a way that the whole
255 complex must dissociate for the glycoprotein to regain its function.
256 The interaction between Fu2 and the RBD is highly unusual, and for a monomer to induce
257 antigen dimerization in this manner, two copies of an antigen must be bound at different epitopes
258 with precisely the right spatial arrangement. This novel mode of antigen binding may be
259 uncommon in naturally elicited antibody repertoires but could be achievable by structure-based
260 antibody design and might present a general strategy for potent immobilization of viral
261 glycoproteins and other antigens. It remains to be seen whether 'designer' bispecific monomer
262 nanobodies can push the potency envelope beyond what is currently attainable.
263
264

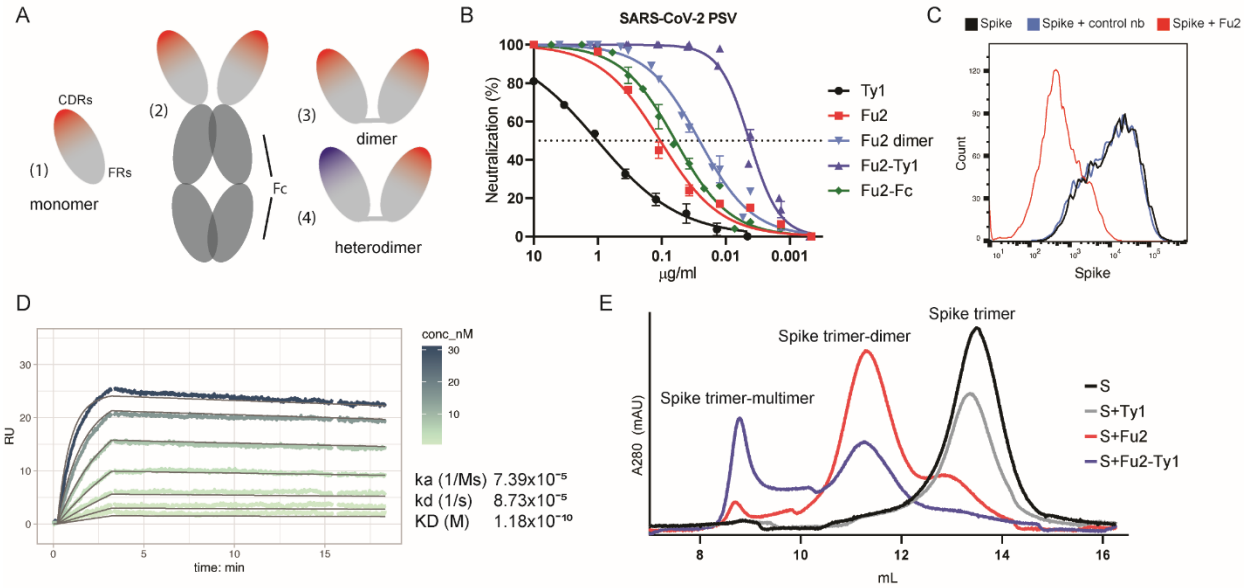

Fig. 1. An RBD-specific nanobody neutralizes SARS-CoV-2. (**A**) Overview of different nanobody constructs used in this study: (1) nanobody monomer, (2) nanobody Fc-fusion, (3) chemically linked nanobody homodimer, (4) chemically linked nanobody heterodimer. (**B**) A SARS-CoV-2 spike pseudotyped lentivirus (PSV) was incubated with a dilution series of the indicated nanobodies at 37°C for one hour before infecting HEK293T-hACE2 cells. Neutralization (in %) compared to untreated PSV is shown. Data from at least two replicates is shown and the error bars represent the standard deviation. (**C**) Recombinantly expressed, prefusion stabilized, and fluorescently labeled SARS-CoV-2 spike protein was incubated with a control nanobody specific for IAV NP [29], or Fu2 and used to stain ACE2 expressing HEK293T cells. Cells were analyzed by flow cytometry and a representative histogram is shown. (**D**) Binding kinetics of Fu2 to the RBD were measured by surface plasmon resonance (SPR). Sensorgram is color-coded based on concentration. The fit is based on the 1:1 Langmuir model and is shown in dark grey solid lines. (**E**) Recombinantly expressed, prefusion stabilized SARS-CoV-2 spike protein was run alone or preincubated with the indicated nanobody constructs on a Superose 6 size-exclusion column. Elution profiles (A280) are shown.

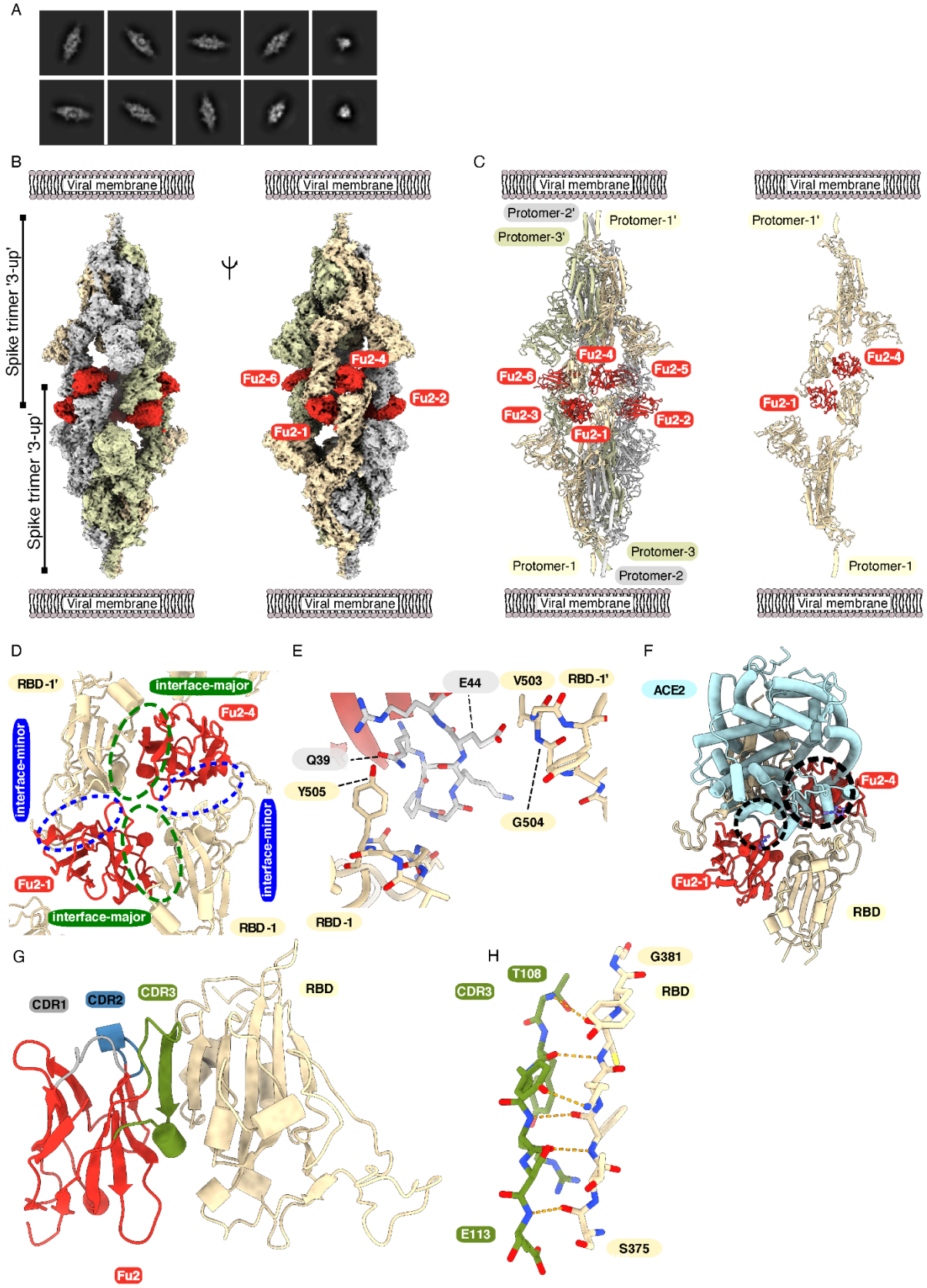
A
B
Viral membrane
Spike trimer '3-up'
Spike trimer '3-up'
Fu2-4
Fu2-6
Fu2-2
Fu2-1
C
Protomer-2'
Protomer-1'
Protomer-3'
Fu2-4
Fu2-6
Fu2-5
Fu2-3
Fu2-2
Fu2-1
Protomer-1
Protomer-3
Protomer-2
Protomer-1'
Fu2-4
Fu2-1
Protomer-1
D
RBD-1'
interface-major
Fu2-4
interface-minor
interface-minor
Fu2-1
interface-major
RBD-1
E
E44
V503
RBD-1'
Q39
Y505
G504
RBD-1
F
ACE2
Fu2-4
Fu2-1
RBD
G
CDR1
CDR2
CDR3
RBD
Fu2
H
T108
G381
CDR3
RBD
E113
S375

282

Fig. 2. Cryo-EM provides structural evidence of Fu2-mediated dimerization of trimeric spike in '3-up' conformation (**A**) Representative 2D class averages. (**B**) Cryo-EM map (two different side views) and (**C**) Atomic model of 'dimeric' spike in complex with Fu2; and two opposite protomers with two Fu2 molecules. Both spike trimers in the complex are present in '3-up' conformation (six Fu2 molecules are numbered). (**D**) Close-up view of the RBD-Fu2 interaction interfaces showing the interface-major and interface-minor. (**E**) A β-hairpin (gray sticks) from the Fu2 framework region (residues 39-45) contacts two RBDs simultaneously in the Fu2-mediated spike trimer-dimer. (**F**) Modelling of simultaneous spike-Fu2-ACE2 binding shows that Fu2 blocks the binding of ACE2 to the RBD from two directions. Clashes marked with dashed circles. (**G**) Fu2 binds the RBD through an extended inter-chain β-sheet interaction mediated by the CDR3 region (green). CDR1 (gray) and CDR2 (blue) does not take part in RBD binding (**H**) Closeup of a part of the CDR3-RBD interface displaying the anti-parallel β-strand hydrogen bond pairing between the Fu2 CDR3 region and the RBD (light orange).

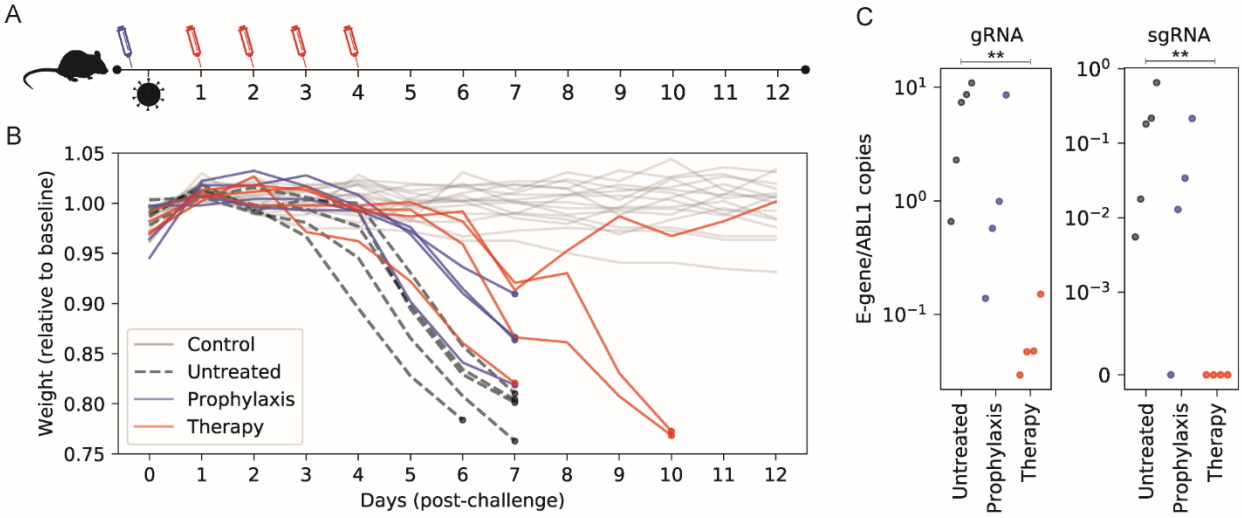

Fig. 3. Therapeutic nanobody reduces disease severity in a SARS-CoV-2 challenge model. (**A**) Timeline of the challenge experiment. K18-hACE2 transgenic mice were challenged with 1000 plaque forming units (PFU) of SARS-CoV-2 and received prophylactic (blue) or therapeutic (red) Fu2-Ty1 at the indicated time points. (**B**) Weight of mice during the challenge experiment. The mean weight of each mouse of day 0 to day 2 served as baseline and the weight loss relative this baseline is shown. Uninfected mice are shown in grey, untreated infected mice in black, prophylactic treatment group in blue and therapeutic group in red. (**C**) Analysis of oropharyngeal samples from mice at day 6 in infected groups. Ratios of E-gene to ABL1 is shown for both genomic and subgenomic RNA (** $p < 0.01$, Mann–Whitney U test, one-tailed).

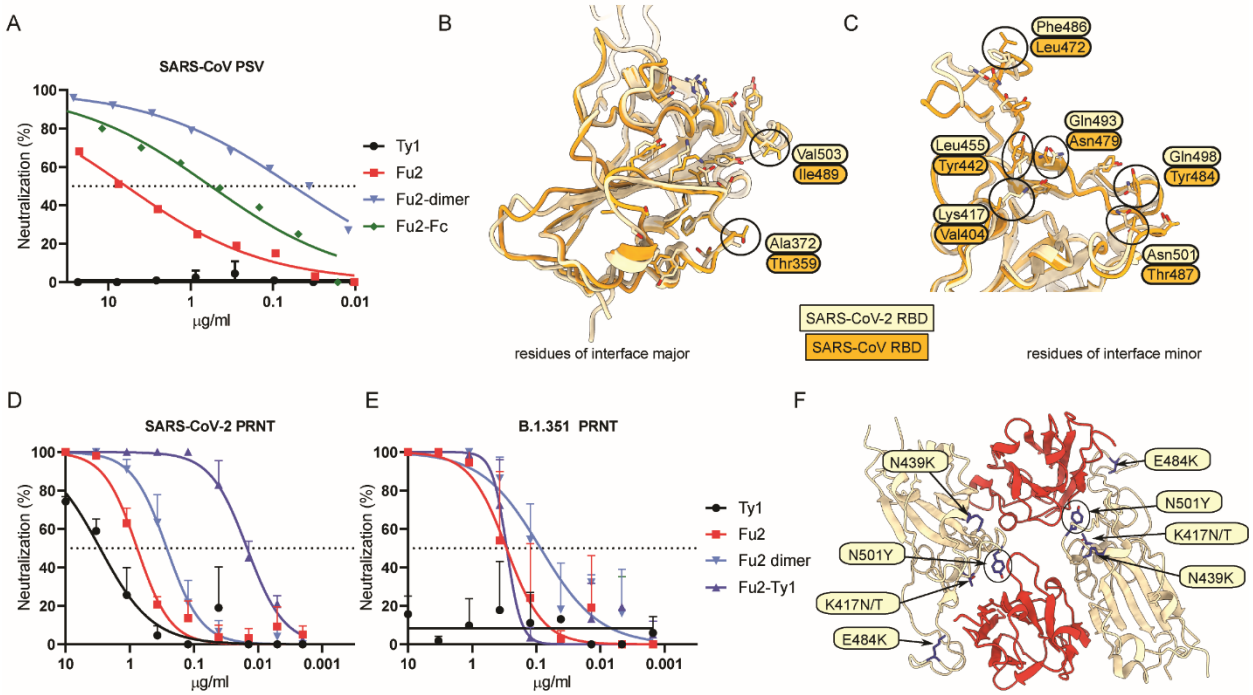

Fig. 4. Fu2 cross-neutralizes SARS-CoV and a B.1.351 variant of concern clinical isolate (**A**) SARS-CoV S pseudotyped lentivirus (PSV) was incubated with the indicated constructs before infecting HEK293T-ACE2 cells, and neutralization is shown compared to untreated PSV. (**B** and **C**) Structural basis of SARS-CoV cross-neutralization by Fu2. Structural alignment of SARS-CoV-2 Spike (RBD bound Fu2) with SARS-CoV RBD (PDB:6ACD). Residues of interface-major and interface-minor shown as sticks, divergent residues are labelled. (**D and E**) PRNTs with clinical isolates of SARS-CoV-2. 100 plaque forming units (PFU) of SARS-CoV-2 [18] or B.1.351 (501Y.V2) [1] were incubated with dilution series of the indicated nanobody constructs for 1 h at 37°C before infecting monolayers of Vero E6 cells. Plaques were quantified 72 h post infection. Neutralization representing the reduction of plaques relative to the control wells is shown. Error bars represent standard deviation (SD) across replicate experiments. (**F**) Assessment of Fu2-RBD interaction in RBD variants. *In silico* mutational analyses of RBD residues and probable impact on Fu2 binding. Fu2 is shown in red and variant residues are indicated.

340 **Materials and Methods**

341

342 **Cells and viruses.**

343 HEK293T cell (ATCC-CRL-3216) and Vero E6 cells (ATCC-CRL-1586) were maintained in
344 DMEM (Gibco) supplemented with 10% fetal calf serum and 1% penicillin-streptomycin in a
345 humidified incubator with 5% CO_2 at 37°C. The HEK293T cell line was further engineered to
346 overexpress human ACE2 by lentiviral transduction [14]. All cell lines used for the experiments
347 were negative for mycoplasma as determined by PCR. Infectious SARS-CoV-2 [18] and the
348 B.1.351 [1] isolate were propagated in Vero E6 cells and titrated by plaque assay.

349

350 **Proteins and probes.**

351 The plasmid for the expression of the SARS-CoV-2 prefusion-stabilized spike (2P) ectodomain
352 was a kind gift from the McLellan lab [6]. The plasmid was used for transient transfection of
353 FreeStyle 293F cells using the FreeStyle MAX reagent (Thermo Fisher Scientific). The spike
354 trimer was purified from filtered supernatant on Streptactin XT resin (IBA Lifesciences) or Ni-
355 NTA resin and purified by size-exclusion chromatography on a Superdex 200 (Cytiva). For cryo-
356 EM a similar construct with 6 proline substitutions (S6-P) was used [30], and the protein was
357 purified on His-Pur Ni-NTA resin (Thermo Fisher Scientific) followed by size-exclusion
358 chromatography.

359 The RBD domain was cloned upstream of a sortase A motif (LPETG) and a 6xHIS tag. The
360 plasmid was used for transient transfection of FreeStyle 293F cells as described above. The
361 protein was purified from filtered supernatant on His-Pur Ni-NTA resin followed by size-
362 exclusion chromatography on a Superdex 200.

363 Nanobodies were cloned in the pHEN plasmid with a C-terminal sortase motif (LPETG) and a
364 6xHIS tag. BL21 *E. coli* were transformed with this plasmid, and expression was induced with 1
365 mM IPTG at OD600 = 0.6 and cells were grown overnight at 30 °C. Nanobodies were retrieved
366 from the periplasm by osmotic shock and purified on Ni-NTA resin and size-exclusion
367 chromatography.
368 Sortase A 5M was produced as described before in BL21 *E. coli* and purified by Ni-NTA and
369 size exclusion chromatography [3].
370 Fluorescent spike ectodomain was generated by first attaching dibenzocyclooctyine-*N*-
371 hydroxysuccinimidyl ester (DBCO-NHS) to the spike trimer in a 3:1 molar ratio, before
372 attaching AbberiorStar-635P-azide by click-chemistry. The final product was purified from
373 unreacted DBCO and fluorophore on a PD-10 desalting column.
374 The biotinylated RBD was generated using sortase A and amine-PEG3-biotin as a nucleophile.
375 The reaction was performed with 50 µM RBD, 5 µM sortase A 5M, and 8 mM amine-PEG3-
376 biotin in 50 mM Tris pH 7.5, 150 mM NaCl, for 6 hours at 4 °C. Sortase A and unreacted RBD
377 was removed on Ni-NTA resin and excess nucleophile was removed by two consecutive
378 purifications on PD-10 desalting columns.
379
380 **Dimer generation using click chemistry.**
381 To generate homo- and hetero-dimers, the different nanobodies were first site-specifically
382 functionalized on the C-terminus using sortase A with either an azide or a dibenzocyclooctine
383 (DBCO) as described in detail here [3]. In brief, for functionalization with DBCO, 70 µM of
384 nanobody was incubated with 5 µM sortase A, 8 mM DBCO-amine (Sigma-Aldrich) in 150 mM
385 NaCl, 50 mM Tris pH 7.5 and 10 mM $CaCl_2$ for 3 h at 25 °C. To functionalize the nanobody
386 with an azide, 70 µM of nanobody, was incubated with 5 µM sortase A 5M, 10 mM 3-azido-1-

387 propanamine (Sigma-Aldrich #762016) in 150 mM NaCl, 50 mM Tris pH 7.5 and 10 mM $CaCl_2$
388 for 3 h at 25 °C. In both reactions, unreacted nanobody, sortase A and excess nucleophile were
389 removed using Ni-NTA resin and PD-10 columns or size-exclusion chromatography. The click
390 reaction was initiated by mixing azide and DBCO labeled nanobody in a 1:1 molar ratio for 48 h
391 at 4 °C. Dimers were purified from unreacted monomeric nanobody by size-exclusion
392 chromatography on a Superdex S200 16/600 column (Cytiva).
393
394 **Alpaca immunization, library generation and nanobody isolation.**
395 One adult female alpaca (*Funny*) at PreClinics, Germany, was immunized four times in a 60-day
396 immunization schedule. Each immunization consisted of two injections. For the first
397 immunization, 200 µg of prefusion stabilized spike and 200 µg of S1+S2 domain (Sino
398 Biologicals) was used. Remaining immunizations each consisted of one injection with 200 µg
399 RBD and one injection with 200 µg prefusion stabilized spike, both produced in Freestyle 293F
400 cells as described above. Serum from the final bleed at day 60 neutralized SARS-CoV-2
401 pseudoviruses with an ID50 >20 000. The animal study protocol was approved by the PreClinics
402 animal welfare officer commissioner and registered under the registration No. 33.19-42502-05-
403 17A210 at the Lower Saxony State Office for Consumer Protection and Food Safety—LAVES
404 and is compliant with the Directive 2010/63/EU on animal welfare.
405 The nanobody phage library was generated as described [14]. Phage display was performed on
406 RBD immobilized on magnetic beads.
407
408 **Neutralization assays.**
409 Pseudotyped virus neutralization assay: Pseudotyped viruses were generated by co-transfection
410 of HEK293T cells with plasmids encoding firefly luciferase, a lentiviral packaging plasmid

411 (Addgene cat#8455), and a plasmid encoding either the SARS-CoV or SARS-CoV-2 spike
412 protein, both harboring a C-terminal truncation of 18 amino acids. Media was changed 12-16 h
413 post-transfection, and pseudotyped viruses were harvested at 48 and 72 hours, filtered through a
414 0.45 µm filter and stored at -80 °C until use. Pseudotyped viruses sufficient to generate 100,000
415 relative light units (RLU) were incubated with serial dilutions of nanobody for 60 min at 37 °C.
416 15,000 HEK293T-ACE2 cells were then added to each well, and the plates were incubated for 48
417 h at 37 °C. Luminescence was measured using Bright-Glo (Promega) on a GM-2000
418 luminometer (Promega) with an integration time of 0.3 s.
419 Plaque reduction neutralization test: One day before the experiment, 100,000 Vero E6 cells were
420 seeded per well of a 24-well plate. A 3-fold serial dilution of the nanobody constructs starting at
421 10 µg/ml were incubated with 100 plaque-forming units (PFU) of the first Swedish clinical
422 isolate of SARS-CoV-2 or variant B.1.351 for 1 h at 37°C. The nanobody-virus mixture was then
423 added to the cells and incubated at 37 °C for 1 h. Cells were washed with PBS, and an overlay of
424 1% CMC/DMEM supplemented with 2% FBS was pipetted into the wells. Three days post-
425 infection, cells were fixed in 10% formaldehyde, followed by staining with crystal violet.
426 Plaques were counted and inhibition determined by comparing to control wells on the same
427 plate.
428
429 **Flow cytometry**
430 HEK293T-hACE2 cells were trypsinized and fixed in 4% formaldehyde in PBS for 20 min. Cells
431 were stained with spike- AbberiorStar-635P not premixed or premixed with Fu2 or control
432 nanobody. Fluorescence was quantified using a BD FACSCelesta and the FlowJo software
433 package.
434

435 **Gel shift assays**

436 For gel shift assay, 80 µg of prefusion stabilized spike protein was incubated with or without
437 nanobody for 15 minutes and was run on a Superose 6 increase 10/300 GL (Cytiva), and
438 absorbance at 280 nm was detected. Sample and injection volumes were kept identical between
439 runs to obtain comparable elution profiles.

440

441 **Next generation sequencing**

442 Next generation sequencing on pre- and post-enrichment nanobody libraries was performed as
443 described in Hanke et al. 2020 [14] on an Illumina MiSeq.

444

445

446 **Surface plasmon resonance**

447 Binding kinetics were determined by surface plasmon resonance using a Biacore 2000. All
448 experiments were performed at 25 °C in a running buffer of 10 mM HEPES, 150 mM NaCl, pH
449 7.4, and 0.005% Tween-20 (v/v). Site-specifically biotinylated RBD was immobilized on
450 streptavidin sensor chips (Series S sensor Chip SA, GE Healthcare) to a level of ~200 resonance
451 units (RU). A 2-fold dilution series of the nanobodies was injected at a flow rate of 30 µl/min
452 (association 180 s, dissociation 900 s), and the immobilized RBD was regenerated using 0.1 M
453 glycine-HCL buffer pH 2 for 2x 10 seconds. Data were analyzed using BIAevaluation Software
454 and fitted using the 1:1 Langmuir model with mass transfer.

455

456 **SARS-CoV-2 challenge experiments**

457 K18-hACE2 transgenic mice were purchased from Jackson laboratories and maintained as a
458 hemizygous line. Experiments were conducted in BSL3 facilities at the Comparative Medicine

459 department (KM-F) at Karolinska Institutet. Ethics for studies of virus infection and therapeutic
460 intervention were obtained from Stockholms Jordbruksverket (10513-2020). Mice were
461 prophylactically or therapeutically administered nanobodies as described in the main text and
462 challenged intranasally with 1000 PFU SARS-CoV-2 (Swedish isolate) in 40 µl PBS following
463 isoflurane sedation. Oropharyngeal sampling was performed at the indicated timepoints under
464 light anesthesia with isoflurane. Weight and general body condition was monitored daily until
465 weight drop started, whereupon mice were monitored twice daily. During the experiment, weight
466 loss, changes in general health, breathing, body movement and posture, piloerection and eye
467 health were monitored. Mice were typically sacrificed when they achieved 20% weight loss.
468 However, some mice were sacrificed before losing 20% in body weight, when movement was
469 greatly impaired and/or they experienced difficulty breathing that was considered to reach a
470 severity level of 0.5 on Karolinska Institutet's veterinary plan for monitoring animal health.
471

472 **RNA Extraction and RT-qPCR for SARS-CoV-2 detection.**

473 Viral RNA was isolated from buccal swabs collected on dpi 6 and stored in 500 µl of TRIzol™
474 Reagent (Invitrogen). Total RNA extractions from buccal swab samples were performed using
475 an adapted TRIzol™ manufacturers protocol with a 45 min precipitation step at -20° C. RNA
476 pellets were resuspended in 20 µl of RNase-free water.
477 RT-PCR reactions were performed using 4 µl of resuspended RNA in a 20 µl reaction volume
478 using the Superscript III one step RT-qPCR system with Platinum Taq Polymerase (Invitrogen)
479 with 400 nM concentrations of each primer and 200 nM of probe. Primers and probes for the
480 CoV-E gene target were as previously described [31]. Primers and probes for the ABL1 target were
481 adapted from Ishige et al. [32] to enable detection of the murine homolog: (ABL1_ENF1003_deg:
482 5'-TGGAGATAACACTCTCAGCATKACTAAAGGT-3', ABL1_ENR1063: 5'-

483 GATGTAGTTGCTTGGGACCCA-3', ABL1_ENPr1043_deg: 5'-HEX-
484 CCATTTTTSGTTTGGGCTTCACACCATT-BHQ1-3'). The CoV-E and ABL1 TaqMan assays
485 were run in multiplex. Detection of the subgenomic CoV-E target was adapted from Wölfel et al.
486 [33], using a leader/E gene junction specific forward primer: (sgEjunc_SARSCoV2_F: 5'-
487 CGATCTCTTGTAGATCTGTTCTCTAAACG-3'). All oligonucleotides were synthesized by
488 Eurofins Genomics.
489 Thermal cycling conditions for all assays consisted of RT at 55 °C for 10m, denaturation at 95
490 °C for 3m, and 45 cycles of 95C, 15s and 58C, 30s. Reactions were carried out using a CFX96
491 Connect Real-Time PCR Detection System (Bio-Rad) following manufacturer instructions. To
492 generate standard curves, a synthetic DNA template gBlock (Integrated DNA Technologies) was
493 transcribed using the mMessage mMachine™ T7 Transcription Kit (Invitrogen) and serially
494 diluted. To reduce sampling-related variability, SARS-CoV-2 RNA copies were normalized by
495 ABL1 copies, and this ratio was used for comparisons. ABL1 copies were not significantly
496 different between groups.
497
498 **Cryo-EM sample preparation and imaging**
499 Spike trimer (1.8mg/ml) S6-P and Fu2 (2.1mg/ml) were mixed in a 1:6 molar ratio followed by
500 incubation on ice for 10 minutes. Prior to cryo-EM grid preparation, grids were glow-discharged
501 with 25 mA for 2 minutes using an EMS 100X (Electron Microscopy Sciences) glow-discharge
502 unit. CryoMatrix® holey grids with amorphous alloy film (R 2/1 geometry; Zhenjiang Lehua
503 Technology Co., Ltd) were used. 3 µl aliquots of sample solutions were applied to the grids and
504 the grids with sample were then vitrified in a Vitrobot Mk IV (Thermo Fisher Scientific) at 4°C
505 and 100% humidity (blot 10 s, blot force 3, 595 filter paper (Ted Pella Inc.)). Cryo-EM data
506 collection was performed with EPU (Thermo Fisher Scientific) using a Krios G3i transmission-

electron microscope (Thermo Fisher Scientific) operated at 300 kV in the Karolinska Institutet's 3D-EM facility (https://ki.se/cmb/3d-em). Images were acquired in 165 kx nanoprobe EFTEM SA mode with a slit width of 10 eV using a K3 Bioquantum during 1.5 s during which 60 movie frames were collected with a flux of 0.81 e-/Å2 per frame (Supplementary Table 1). Motion correction, CTF-estimation, Fourier binning (to 1.01 Å/px), picking and extraction in 600-pixel boxes (size threshold 400 Å, distance threshold 100 Å, using the pretrained BoxNet2Mask_20180918 model) were performed on the fly using Warp [34]. Due to preferential orientation, we collected a part of the dataset with 25-degree stage tilt.

A total of 14,081 micrographs were selected based on an estimated resolution cut-off of 4 Å and defocus below 2 microns as estimated by Warp. Furthermore, Warp picked 1,035,962 particles (dimer of trimeric spike with Fu2) based on above-mentioned criteria. Extracted particles were imported into cryoSPARC v3.0.1 [35] for 2D classification, 3D classification and non-uniform 3D refinement. After 2D classification, clean classes with high-resolution features (and with characteristic trimeric spike views) were retained and used to generate ab-initio 3D reconstructions. In total 277,372 particles were retained for refinement steps and these particles were processed with C1 symmetry (image processing scheme Supplementary Fig. 5).

These particles were further processed using heterogeneous refinement that resulted in a reconstruction with high-resolution structural features in the core of the spike. One round of homogeneous refinement was followed by non-uniform refinement. All final reconstructions were analysed using 3D-FSC [36] and there were moderate anisotropy in the full map reconstructions while the localized reconstruction displayed no significant anisotropy (Supplementary Fig. 6A and 6B). All CTF refinements were per-particle CTF refinements interspersed with global aberration correction (beamtilt, trefoil, tetrafoil and spherical aberration). Please see Supplementary Table 1 for data collection and processing statistics and

531 the respective cryo-EM data processing schemes. For the Spike-Fu2 dimer interface we used a
532 particle set with partial-signal subtraction of all parts except for Fu2-RBD dimer interface
533 (containing two RBDs and two Fu2). From this we performed local reconstruction (non-
534 uniform). The local reconstruction resulted in a map with 2.89Å overall resolution as compared
535 to 3.2Å overall resolution for the full map.
536
537 **Cryo-EM model building and structure refinement**
538 The structure of the spike protein trimer PDB: 7KSG [5] was used as a starting model for model
539 building. A homology model for Fu2 was generated by swiss model [37] with PDB: 5LHN as
540 template (chain B) [38]. Structure refinement and manual model building were performed using
541 COOT [39] and PHENIX [40] in interspersed cycles with secondary structure, Ramachandran,
542 rotamers and bond geometry restrains. Structure figures and EM density-map figures were
543 generated with UCSF ChimeraX [41] and COOT, respectively. Please see Supplementary Table 2
544 for refinement and validation statistics.
545
546 **References**
547 1. Cele, S. *et al.* Escape of SARS-CoV-2 501Y.V2 from neutralization by convalescent plasma.
548 *medRxiv* 2021.01.26.21250224 (2021) doi:10.1101/2021.01.26.21250224.
549 2. Muyldermans, S. Nanobodies: Natural Single-Domain Antibodies. *Annu. Rev. Biochem.* **82**, 775–
550 797 (2013).
551 3. Moliner-morro, A. *et al.* Picomolar SARS-Cov-2 neutralization using multi-arm PEG nanobody
552 constructs. *Biomolecules* **10**, 1–11 (2020).
553 4. Hultberg, A. *et al.* Llama-derived single domain antibodies to build multivalent, superpotent and
554 broadened neutralizing anti-viral molecules. *PLoS One* **6**, 1–12 (2011).

555 5. Koenig, P.-A. *et al.* Structure-guided multivalent nanobodies block SARS-CoV-2 infection and
556 suppress mutational escape. *Science (80-.).* **371**, eabe6230 (2021).
557 6. Wrapp, D. *et al.* Cryo-EM structure of the 2019-nCoV spike in the prefusion conformation.
558 *Science (80-.).* **367**, (2020).
559 7. Walls, A. C. *et al.* Structure, Function, and Antigenicity of the SARS-CoV-2 Spike Glycoprotein. *Cell*
560 **181**, 281-292.e6 (2020).
561 8. Walls, A. C. *et al.* Unexpected Receptor Functional Mimicry Elucidates Activation of Coronavirus
562 Fusion. *Cell* **176**, 1026-1039.e15 (2019).
563 9. Pallesen, J. *et al.* Immunogenicity and structures of a rationally designed prefusion MERS-CoV
564 spike antigen. *Proc. Natl. Acad. Sci. U. S. A.* **114**, E7348–E7357 (2017).
565 10. Wang, C. *et al.* A human monoclonal antibody blocking SARS-CoV-2 infection. *Nat. Commun.* **11**,
566 1–6 (2020).
567 11. Liu, L. *et al.* Potent neutralizing antibodies against multiple epitopes on SARS-CoV-2 spike. *Nature*
568 **584**, 450–456 (2020).
569 12. Lei, C. *et al.* Neutralization of SARS-CoV-2 spike pseudotyped virus by recombinant ACE2-Ig. *Nat.*
570 *Commun.* **11**, (2020).
571 13. Custódio, T. F. *et al.* Selection, biophysical and structural analysis of synthetic nanobodies that
572 effectively neutralize SARS-CoV-2. *Nat. Commun.* **11**, (2020).
573 14. Hanke, L. *et al.* An alpaca nanobody neutralizes SARS-CoV-2 by blocking receptor interaction. *Nat.*
574 *Commun.* **11**, 4420 (2020).
575 15. Xiang, Y. *et al.* Versatile and multivalent nanobodies efficiently neutralize SARS-CoV-2. *Science*
576 *(80-.).* **370**, 1479–1484 (2021).
577 16. Schoof, M. *et al.* An ultrapotent synthetic nanobody neutralizes SARS-CoV-2 by stabilizing
578 inactive Spike. *Science (80-.).* **370**, 1473–1479 (2021).
579 17. Ibañez, L. I. *et al.* Nanobodies with in vitro neutralizing activity protect mice against H5N1

580 influenza virus infection. *J. Infect. Dis.* **203**, 1063–1072 (2011).

581 18. Monteil, V. *et al.* Inhibition of SARS-CoV-2 Infections in Engineered Human Tissues Using Clinical-
582 Grade Soluble Human ACE2. *Cell* **181**, 905-913.e7 (2020).

583 19. Cardoso, F. M. *et al.* Single-Domain Antibodies Targeting Neuraminidase Protect against an H5N1
584 Influenza Virus Challenge. *J. Virol.* **88**, 8278–8296 (2014).

585 20. Power, U. F., Stortelers, C., Allosery, K. & Melero, J. A. Generation and Characterization of ALX-
586 0171 , a Potent Novel Therapeutic Nanobody for the Treatment of Respiratory Syncytial Virus
587 Infection. *Antimicrob. Agents Chemother.* **60**, 6–13 (2016).

588 21. Planas, D. *et al.* Sensitivity of infectious SARS-CoV-2 B.1.1.7 and B.1.351 variants to neutralizing
589 antibodies. doi:10.1101/2021.02.12.430472.

590 22. Tada, T. *et al.* Neutralization of viruses with European, South African, and United States SARS-
591 CoV-2 variant spike proteins by convalescent sera and BNT162b2 mRNA vaccine-elicited
592 antibodies. doi:10.1101/2021.02.05.430003.

593 23. Hu, J. *et al.* Emerging SARS-CoV-2 variants reduce neutralization sensitivity to convalescent sera
594 and monoclonal antibodies. *Cell. Mol. Immunol.* 1–3 (2021) doi:10.1038/s41423-021-00648-1.

595 24. Wrapp, D. *et al.* Structural Basis for Potent Neutralization of Betacoronaviruses by Single-Domain
596 Camelid Antibodies. *Cell* **181**, 1004-1015.e15 (2020).

597 25. Cortez-Retamozo, V. *et al.* Efficient tumor targeting by single-domain antibody fragments of
598 camels. *Int. J. Cancer* **98**, 456–462 (2002).

599 26. Vieira, P. & Rajewsky, K. The half-lives of serum immunoglobulins in adult mice. *Eur. J. Immunol.*
600 **18**, 313–316 (1988).

601 27. Tijink, B. M. *et al.* Improved tumor targeting of anti-epidermal growth factor receptor
602 Nanobodies through albumin binding: Taking advantage of modular Nanobody technology. *Mol.*
603 *Cancer Ther.* **7**, 2288–2297 (2008).

604 28. Bangaru, S. *et al.* Structural analysis of full-length SARS-CoV-2 spike protein from an advanced

605 vaccine candidate. *Science (80-.).* **370**, 1089–1094 (2020).

606 29. Hanke, L. *et al.* The Antiviral Mechanism of an Influenza A Virus Nucleoprotein-Specific Single-
607 Domain Antibody Fragment. *MBio* **7**, e01569--16 (2016).

608 30. Hsieh, C. L. *et al.* Structure-based design of prefusion-stabilized SARS-CoV-2 spikes. *Science (80-.*
609 *).* **369**, 1501–1505 (2020).

610 31. Corman, V. M. *et al.* Detection of 2019 novel coronavirus (2019-nCoV) by real-time RT-PCR.
611 *Eurosurveillance* **25**, 2000045 (2020).

612 32. Ishige, T. *et al.* Highly sensitive detection of SARS-CoV-2 RNA by multiplex rRT-PCR for molecular
613 diagnosis of COVID-19 by clinical laboratories. *Clin. Chim. Acta* **507**, 139–142 (2020).

614 33. Wölfel, R. *et al.* Virological assessment of hospitalized patients with COVID-2019. *Nature* **581**,
615 465–469 (2020).

616 34. Tegunov, D. & Cramer, P. Real-time cryo-electron microscopy data preprocessing with Warp. *Nat.*
617 *Methods* **16**, 1146–1152 (2019).

618 35. Punjani, A., Rubinstein, J. L., Fleet, D. J. & Brubaker, M. A. CryoSPARC: Algorithms for rapid
619 unsupervised cryo-EM structure determination. *Nat. Methods* **14**, 290–296 (2017).

620 36. Zi Tan, Y. *et al.* Addressing preferred specimen orientation in single-particle cryo-EM through
621 tilting. *Nat. Methods* **14**, 793–796 (2017).

622 37. Waterhouse, A. *et al.* SWISS-MODEL: Homology modelling of protein structures and complexes.
623 *Nucleic Acids Res.* (2018) doi:10.1093/nar/gky427.

624 38. Kromann-Hansen, T. *et al.* Discovery of a novel conformational equilibrium in urokinase-type
625 plasminogen activator. *Sci. Rep.* **7**, 1–11 (2017).

626 39. Emsley, P., Lohkamp, B., Scott, W. G. & Cowtan, K. Features and development of Coot. *Acta*
627 *Crystallogr. Sect. D Biol. Crystallogr.* **66**, 486–501 (2010).

628 40. Adams, P. D. *et al.* PHENIX: A comprehensive Python-based system for macromolecular structure
629 solution. *Acta Crystallogr. Sect. D Biol. Crystallogr.* **66**, 213–221 (2010).

630 41. Goddard, T. D. *et al.* UCSF ChimeraX: Meeting modern challenges in visualization and analysis.
631 *Protein Sci.* **27**, 14–25 (2018).
632 42. Chen, V. B. *et al.* MolProbity: All-atom structure validation for macromolecular crystallography.
633 *Acta Crystallogr. Sect. D Biol. Crystallogr.* **66**, 12–21 (2010).
634 43. Barad, B. A. *et al.* EMRinger: Side chain-directed model and map validation for 3D cryo-electron
635 microscopy. *Nat. Methods* **12**, 943–946 (2015).
636
637
638
639
640

Acknowledgments: Experiments with replication-competent SARS-CoV-2 were performed in the Biomedicum BSL3 core facility, Karolinska Institutet. All cryo-EM data were collected in the Karolinska Institutet 3D-EM facility. We thank Agustin Ure for assistance with figure generation and Tomas Nyman (Protein Science Facility at KI) for providing access to SPR instruments.

Funding: LH was supported by the David och Astrid Hageléns stiftelse, the Clas Groschinskys Minnesfond and a Jonas Söderquist's scholarship. This project has received funding from the European Union's Horizon 2020 research and innovation program under grant agreement No. 101003653 (CoroNAb), to BM and GMM. BMH is supported by the Knut and Alice Wallenberg Foundation (KAW 2017.0080 and KAW 2018.0080). The work was supported by project grants from the Swedish Research Council to BMH (2017-6702 and 2018-3808), BM (2018-02381) and to GMM (2018-03914 and 2018-03843).

Author contributions: Conceptualization: LH, BM, GMM. Methodology: LH, DJS, JMC, BMH, BM, GMM. Investigation: LH, HD, DJS, LPV, EU, AMM, VK, NS, AP, CK, GKP, BMH. Data Curation: LH, BM. Visualization: LH, HD, BHM, BM. Funding acquisition: LH, BMH, BM, GMM. Supervision: LH, DJS, JMC, BM, GMM. Writing – original draft: LH, HD. Writing – review & editing: LH, HD, DJS, LPV, EU, AMM, VK, GKP, JMC, BMH, BM, GMM.

Competing interests: LH, DJS, LPV, BM, and GMM are listed as inventors on a patent application describing SARS-CoV-2 nanobodies.

Data and materials availability: The cryo-EM density maps have been deposited in the Electron Microscopy Data Bank under accession codes EMD-12561 (dimer of spike trimer + 6 Fu2) and EMD-12465 (localized reconstruction of 2 RBDs + 2 Fu2). The atomic coordinates have been deposited in the Protein Data Bank under IDs 7NS6 (dimers of spike trimers + 6 Fu2) and 7NLL (localized reconstruction of 2 RBDs + 2 Fu2). All nanobody sequences will be made available on public databases upon publication.

Supplementary Figures

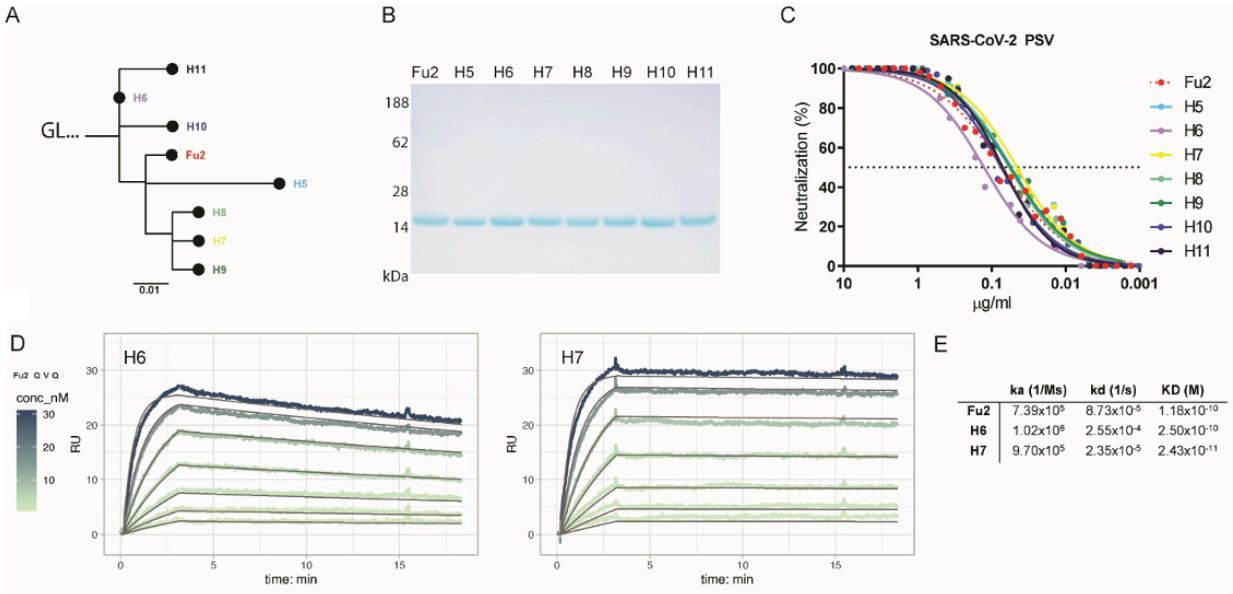

Supplementary Fig. 1. Fu2 variants identified by next-generation sequencing (NGS) display similar neutralization potential and binding kinetics. (**A**) Average difference of Fu2 variants is shown as a tree diagram. (**B**) Fu2 and seven Fu2-variants were expressed in *E.coli*, purified, and analyzed by SDS-PAGE and Coomassie staining. (**C**) A dilution series of Fu2 and its variants were incubated with SARS-CoV-2 pseudotyped lentivirus (PSV) for 1 hour at 37 °C before infecting HEK293T-hACE2 cells. Neutralization (in %) compared to the untreated PSV is shown. (**D**) Binding kinetics of Fu2 and variants to the RBD were measured by surface plasmon resonance (SPR). Site-specifically biotinylated RBD was immobilized on streptavidin sensor chips, and kinetics for a dilution series of the indicated monomeric nanobodies were measured. Sensorgrams are color-coded based on concentration. The fit is based on the 1:1 Langmuir model and is shown in dark grey solid lines. (**E**) Kinetic parameters of Fu2 and Fu2 variants binding to the RBD.

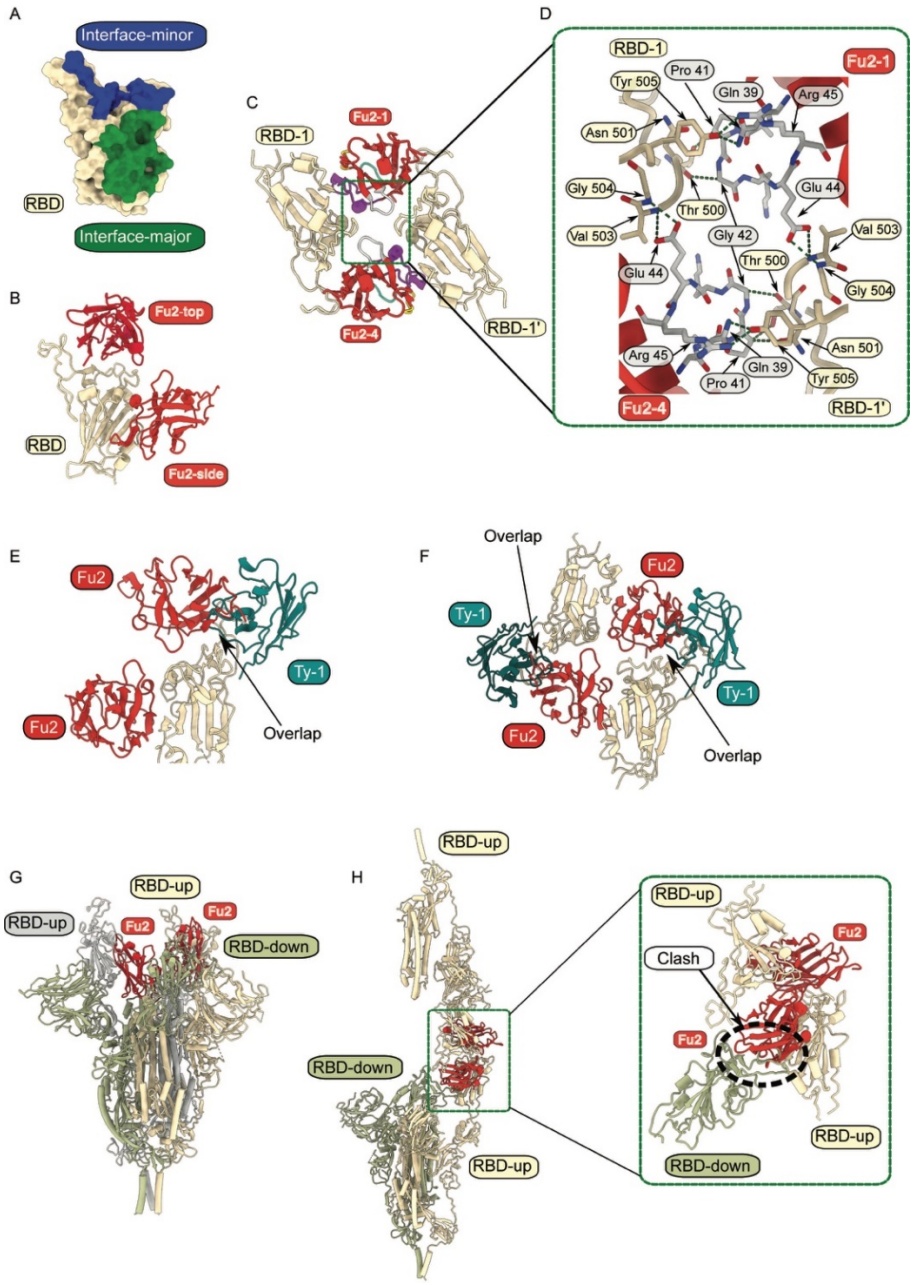

Supplementary Fig. 2. (**A**) Surface view of the RBD with interface-major and interface-minor color coded. (**B**) Relative positions of two Fu2 molecules binding the RBD. (**C**) The interaction between two RBDs and two Fu2s showing in gray the β-hairpins in the Fu2 framework region (39-45) that help to mediate the dimer-of-trimers Fu2-spike complex. (**D**) Close-up view of (C) (**E** and **F**) Assessment of Fu2-Ty1 heterodimer binding. Alignment of the Spike-Fu2 structure to the Spike-Ty1 structure (RBD in 'up' conformation) (PDB:6ZXN). Arrows indicate partial overlap of binding surface on RBD**.** (**G**) Assessment of Fu2-RBD interaction in RBD-down conformation. RBD-Fu2 structure superimposed to RBD-down of spike in 2-up conformation (PDB:7A29) (**H**) Assessment of Fu2-RBD interaction in RBD-down conformation in dimeric spike. 2-up spike (PDB:7A29) is shown superimposed with the spike dimer-of-trimers.

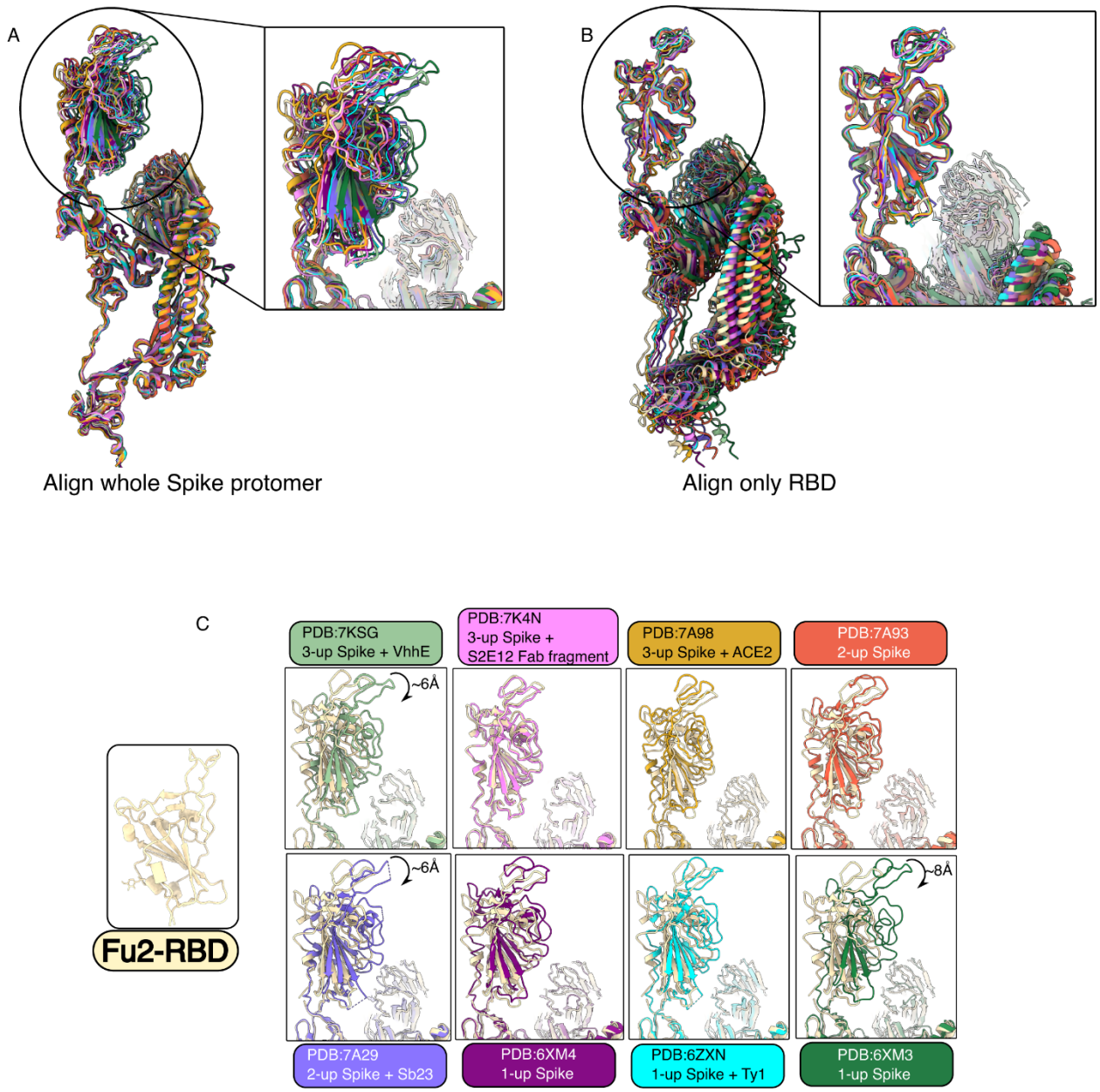

Supplementary Fig. 3. Assessment of Fu2 mediated structural changes in spike structure. (**A**) Alignment of dimeric spike trimer with spikes in 1-up, 2-up and 3-up conformation (one protomer in 'up' state shown). (**B**) Structural alignment of dimeric spike trimer with RBDs of 1-up, 2-up and 3-up spikes (protomer in 'up' conformation). (**C**) Structural comparison of RBD (Fu2-bound dimeric spike) with eight different RBDs structures.

A

```
SARS-CoV-2 RBD  333 TNLCPFGEVFNATRFASVYAWNRKRISNCVADYSVLYNSASFSTFKCYGVSPTKLNDLCF  392
  SARS-CoV RBD  320 TNLCPFGEVFNATKFPSVYAWERKKISNCVADYSVLYNSTFFSTFKCYGVSATKLNDLCF  379
                    *************:* *****:**:**************: ********** ********

SARS-CoV-2 RBD  393 TNVYADSFVIRGDEVRQIAPGQTGKIADYNYKLPDDFTGCVIAWNSNNLDSKVGGNYNYL  452
  SARS-CoV RBD  380 SNVYADSFVVKGDDVRQIAPGQTGVIADYNYKLPDDFMGCVLAWNTRNIDATSTGNYNYK  439
                    :********::**:********** ************ ***:***:.*:*:.  *****

SARS-CoV-2 RBD  453 YRLFRKSNLKPFERDISTEIYQAGSTPC GVEGFNCYFPLQSYGFQPTNGVGYQPYRVVV  512
  SARS-CoV RBD  440 YRYLRHGKLRPFERDISNVPFSPDGKPCT-PPALNCYWPLNDYGFYTTTGIGYQPYRVVV  499
                    ** :*:.:*:*******.  :. ...**.   .:***:**:.***  *.*:*********

SARS-CoV-2 RBD  513 LSFELLHAPATVCGPK  514
  SARS-CoV RBD  500 LSFELLNAPATVCGPK  528
                    ******:*********
```

residues interface-major

residues interface-minor

B

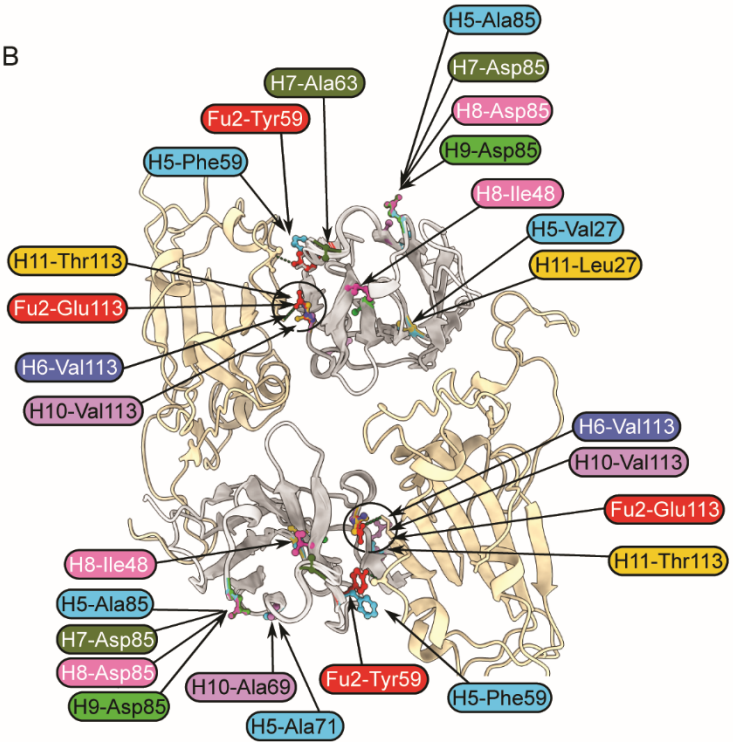

Supplementary Fig. 4. (**A**) Sequence alignment of RBDs from SARS-CoV and SARS-CoV-2. Interface-major and interface-minor residues are highlighted. Arrows indicate the different amino acids of the interface. (**B**) Fu2 variants and analysis of interface residues. Distinct residues of different variants shown as sticks (color coded).

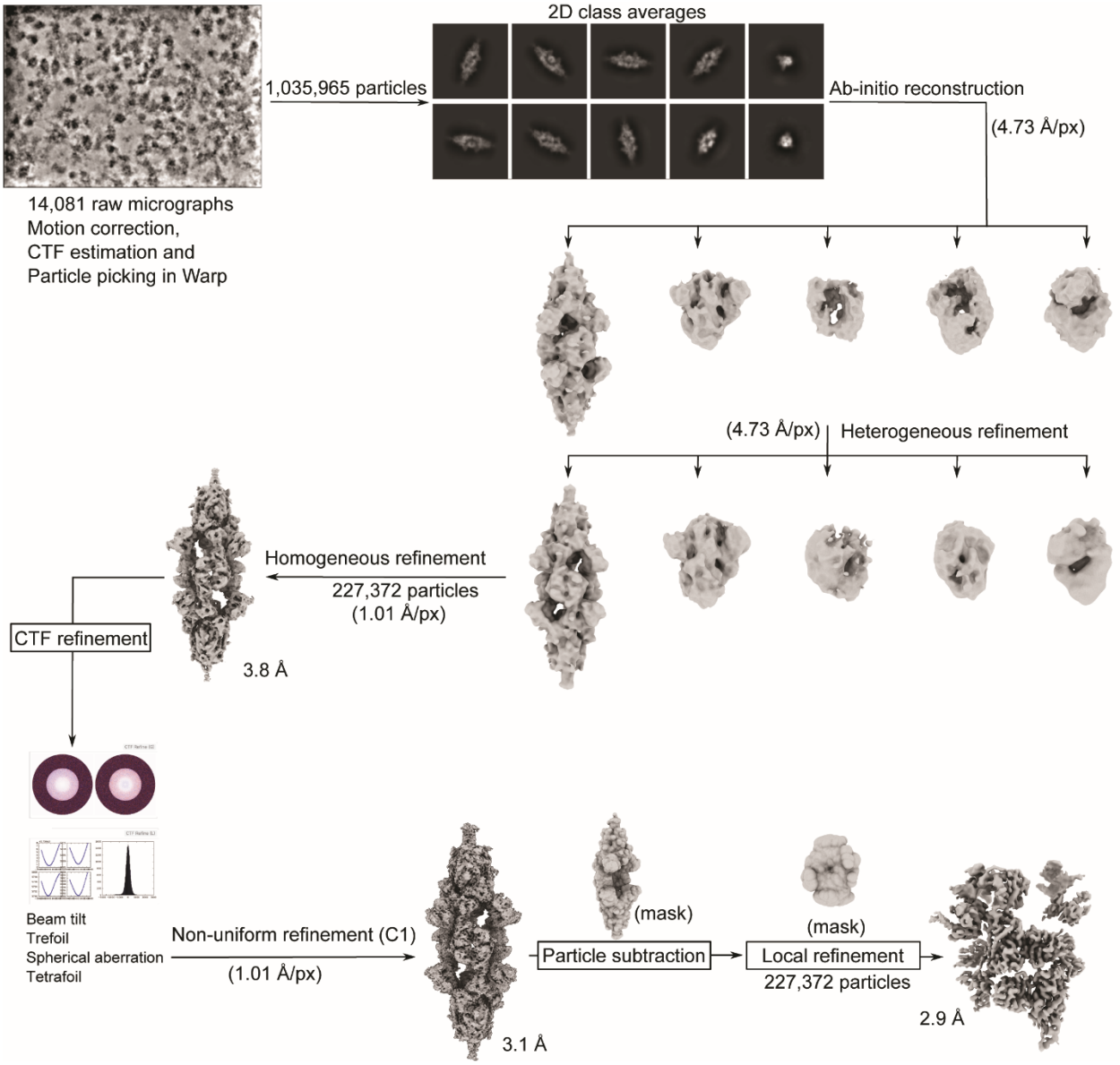

Supplementary Fig. 5 Cryo-EM image processing scheme. Particles picked by Warp were processed in cryoSPARC v3.1. Representative 2D class averages are shown. Particles contributing to the clean classes were used to generate ab-initio reconstructions (five classes) followed by heterogeneous refinement. One class showing high-resolution features was refined further (C1 symmetry). For localized reconstruction, particle subtraction followed by local refinement (Non-uniform) was performed.

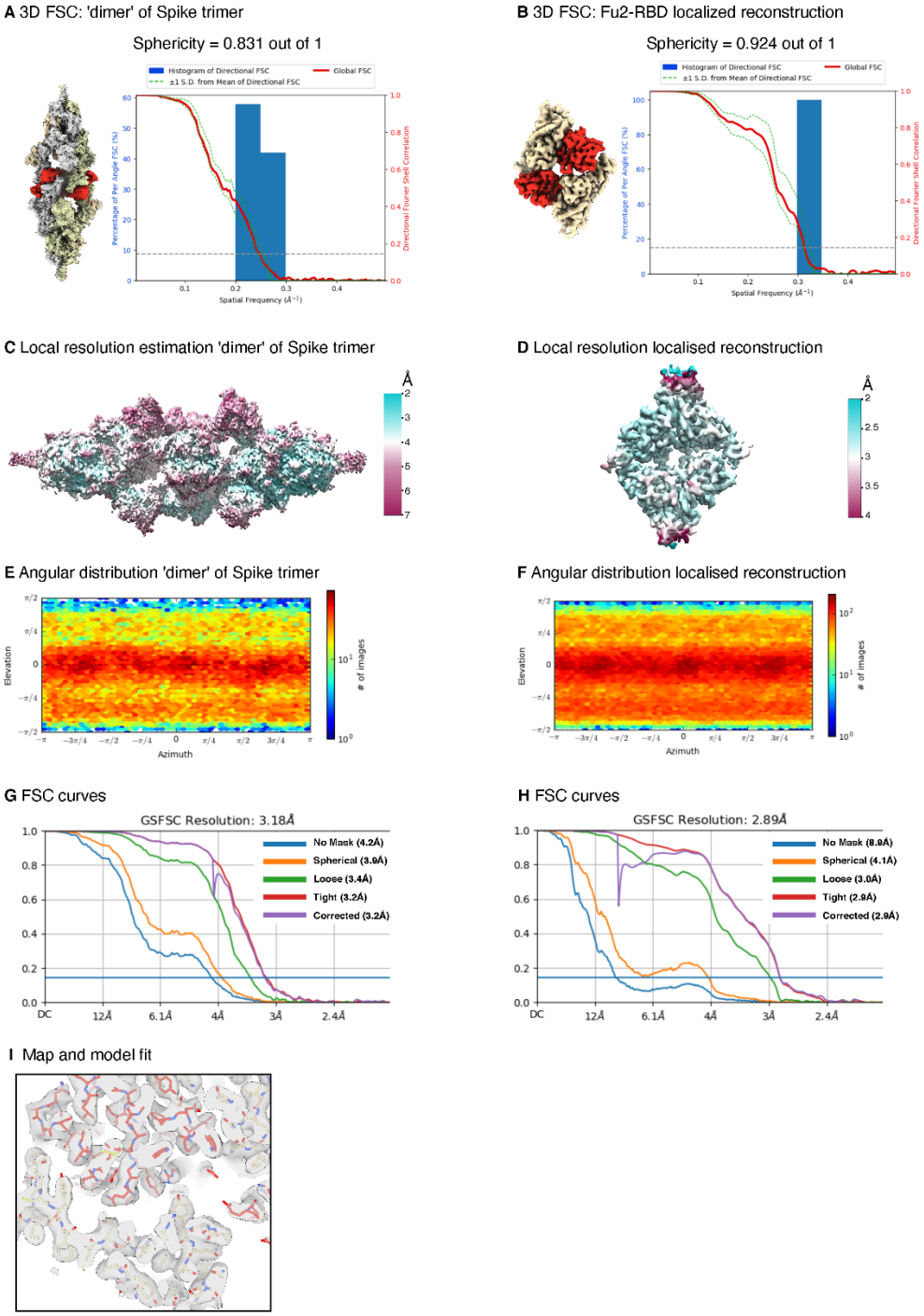

Supplementary Fig. 6 Cryo-EM validation (**A**) and (**B**) 3D FSC and sphericity of 'dimer' of spike trimer and of localized map, (**C**) and (**D**) Local resolution estimation of 'dimer' of spike trimer and local resolution estimation of localized map (**E**) and (**F**) Angular distribution of 'dimer' of spike trimer reconstruction and localized reconstruction map (**G**) and (**H**) FSC curves of 'dimer' of spike trimer and of localized map (**I**) model-map fitting atomic resolution.

732 **Supplementary Table 1. Cryo-EM data collection and processing**

733

	Dimer of spike trimer + 6 Fu2	Localized reconstruction of 2 RBDs + 2 Fu2
EMDB	**EMD-12561**	**EMD-12465**
PDB	**7NS6**	**7NLL**
Data collection		
Microscope	TFS Krios G3i	
Voltage (kV)	300	
Detector	Bioquantum K3	
Recording mode	Counting	
EFTEM SA Magnification	165kx	
Calibrated pixel size (Å)	0.51	
Movie micrograph pixel size (Å)	0.51	
Flux (e^-/[(camera pixel)*s])	8.4	
Number of frames per movie micrographs	60	
Total movie micrograph exposure time (s)	1.5	
Fluency (e^-/Å^2)	48.6	
Underfocus range (µm)	0.2 – 1.3	
Energy filter slit width (eV)	10	
Data collection automation software	EPU	
EM Data processing		
Number of micrographs	14,081	14,081
Number of total projection images	1,035,962	1,035,962
Number of projection images used for reconstruction	277,372	277,372
Symmetry	C1	C1
Map resolution (FSC 0.143; Å)	3.18	2.9
Map resolution no mask (FSC 0.143; Å)	4.2	8.9
B-factor applied to map (Å^2)	68.1	37.3
3D-FSC [36]		
3D-FSC resolution (3D-FSC 0.143; Å)	4.0	3.2
Sphericity (3D-FSC)	0.831	0.924

734

735 **Supplementary Table 2. Cryo-EM model refinement and validation statistics**
736

	Dimer of spike trimers + 6 Fu2	Localized reconstruction of 2 RBDs + 2 Fu2
EMDB	**EMD-12561**	**EMD-12465**
PDB	**7NS6**	**7NLL**
Refinement		
Refinement Package	PHENIX 1.19	PHENIX 1.19
Refinement space	Real	Real
Highest resolution used	3.2	2.9
Model composition		
Atoms refined	55904	5058
Residues SARS-CoV-2 Spike (or RBD) and nanobody Fu2	7109	656
Glycans	50	2
Full Map-model correspondence		
Map correlation coefficient	0.87	0.90
Map to model FSC (Å) (FSC 0.143)	3.2	2.6
Mean B-factor		
Residues SARS-CoV-2 Spike (or RBD) and nanobody Fu2	140	85.89
Glycans	129	96.22
Model geometry		
RMSD ideal bond length (Å)	0.004	0.003
RMSD ideal bond angles (˚)	0.826	0.529
Side chain rotamer outliers (%)	0	0
C-ß outliers (%)	0.38	0
Ramachandran plot		
Favoured (%)	97.76	99.38
Outliers (%)	0	0
General macromolecular model validation		
MolProbity score [42]	1.66	1.38
Clashscore [42]	12.38	6.92
EM specific model validation		
CaBLAM (%) [43]	2.55	0.94
EM-ringer score [43]	1.73	3.16

737
738
739
740